Optical calibration of the SuperCam instrument body unit spectrometers

Carey Legett, Raymond Newell, Adriana Reyes-Newell, Anthony Nelson, Pernelle Bernardi, Steven Bender, Olivier Forni, D Venhaus, Samuel Clegg, A Ollila, et al.

applied optics

Optical calibration of the SuperCam instrument body unit spectrometers

Carey Legett IV,[1,*] Raymond T. Newell,[1] Adriana L. Reyes-Newell,[1]
Anthony E. Nelson,[1] Pernelle Bernardi,[2] Steven C. Bender,[3] Olivier Forni,[4]
D. M. Venhaus,[1] Samuel M. Clegg,[1] A. M. Ollila,[1] Paolo Pilleri,[4] V. Sridhar,[5]
S. Maurice,[4] and Roger C. Wiens[1]

[1]*Los Alamos National Laboratory, P.O. Box 1663, Los Alamos, New Mexico 87545, USA*
[2]*Laboratoire d'Etudes Spatiales et d'Instrumentation en Astrophysique, Observatoire de Paris, CNRS, Sorbonne Univ., Univ. Paris-Diderot,
5 place Jules Janssen, 92195 Meudon Cedex, France*
[3]*Planetary Science Institute, 1700 E. Ft. Lowell, Ste. 106, Tucson, Arizona 85719-2395, USA*
[4]*L'Institut de Recherche en Astrophysique et Planétologie, 9 Av. Du Colonel Roche, 31400 Toulouse, France*
[5]*Jet Propulsion Laboratory/Caltech, 4800 Oak Grove Dr., Pasadena, California 91109, USA*
*Corresponding author: clegett@lanl.gov

The SuperCam remote sensing instrument on NASA's Perseverance rover is capable of four spectroscopic techniques, remote micro-imaging, and audio recording. These analytical techniques provide details of the chemistry and mineralogy of the rocks and soils probed in the Jezero Crater on Mars. Here we present the methods used for optical calibration of the three spectrometers covering the 243–853 nm range used by three of the four spectroscopic techniques. We derive the instrument optical response, which characterizes the instrument sensitivity to incident radiation as a function of a wavelength. The instrument optical response function derived here is an essential step in the interpretation of the spectra returned by SuperCam as it converts the observed spectra, reported by the instrument as "digital counts" from an analog to digital converter, into physical values of spectral radiance.   © 2022 Optica Publishing Group under the terms of the Optica Open Access Publishing Agreement

https://doi.org/10.1364/AO.447680

1. INTRODUCTION

A. SuperCam Instrument Description

The SuperCam instrument on the NASA Perseverance rover provides the capability for laser-induced breakdown spectroscopy (LIBS), Raman spectroscopy, time-resolved luminescence (TRL) spectroscopy, passive reflectance spectroscopy, audio recording, and remote micro-imaging (RMI) [1,2]. LIBS provides remote quantitative elemental abundances [3], while Raman and passive reflectance provide remote determination of mineral phases. TRL spectroscopy provides information about the presence of trace elements (such as rare earth elements) in certain minerals, as well as information about certain defects in mineral structures. SuperCam's design, using a single telescope for the laser and the co-boresighted spectrometers allows for the collection of all these types of data on a single point (with a less than 1 mrad spread; see Fig. 1 below and Fig. 50 of [1]), along with an image of the target. The information gathered from these techniques will help us understand the history of Mars's water, climate, and habitability.

The instrument is split between the mast unit (MU), mounted at the top of the rover's remote sensing mast, and the body unit (BU), located inside the rover's body. The MU and BU are connected by a 5.8 m optical fiber, as well as data and power cables. The MU consists of the telescope, infrared spectrometer (IRS), RMI camera, laser, and associated electronics. The IRS is used for passive reflectance observations at wavelengths from 1.3 to 2.6 μm. Detailed descriptions of its design, testing, and calibration are provided elsewhere [4,5]. This paper details the calibration of only the BU spectrometers, which constitute three of four SuperCam spectrometers, excluding the IRS which resides in the MU. The BU contains an optical demultiplexer to distribute the light from the telescope to the appropriate spectrometer, three spectrometers covering the wavelength ranges from approximately 243–853 nm, a high voltage power supply, and a control and data handling unit. The BU spectrometers are used for LIBS, Raman, TRL, and passive reflectance spectroscopies.

The BU spectrometers are made up of two crossed Czerny–Turner spectrometers (of ChemCam heritage [6]) for the UV (243.5–341.7 nm) and blue-violet (VIO; 382.1–467.5 nm) spectral ranges and an intensified transmission spectrometer for the green, orange, and red (GOR; 535–853 nm) spectral ranges. The transmission spectrometer uses an image intensifier
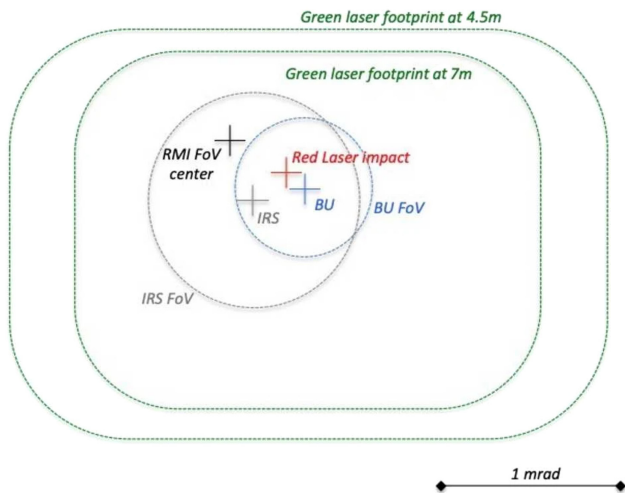
Fig. 1. Co-alignment of SuperCam lasers, spectrometers, and RMI. The FOVs for the three spectrometers discussed in this paper are indicated by the "BU" and "BU FoV" markings. BU, body unit; FoV, field of view. Reproduced unaltered from Figure 50 of [1] under the terms of the Creative Commons CC BY license (https://creativecommons.org/licenses/by/4.0/).

(made by Excelis, now Elbit Systems of America) with selectable amplification. A detailed description of the BU is available in [2].

B. CCD Configuration and Readout

The light entering the instrument is projected onto the 515 rows × 2048 columns pixel CCDs as bands of light with a wavelength corresponding to the longer axis (i.e., columns, Fig. 2). These bands of light are roughly centered on the UV and VIO CCDs (Figs. 2A and 2B), taking up slightly less than 200 rows of pixels. In the GOR spectrometer, the light is split into three bands covering 535–853 nm. The band closest to the CCD serial register is referred to as the "red" region and covers 712–853 nm; the "green" region covering 535–620 nm is in the center, and at the other side of the CCD is the "orange" region covering 620–712 nm (Fig. 2C). The UV and VIO regions are selectable among 16, 40, and 200 rows for on-chip summing. Since the UV and VIO spectrometers lack any kind of shutter, this row-reduction capability allows us to prevent saturation of the analog-to-digital converter when using LIBS on targets at short distances (e.g., calibration targets at 1.5 m). The GOR spectrometer's intensifier has adjustable gain, so it is not
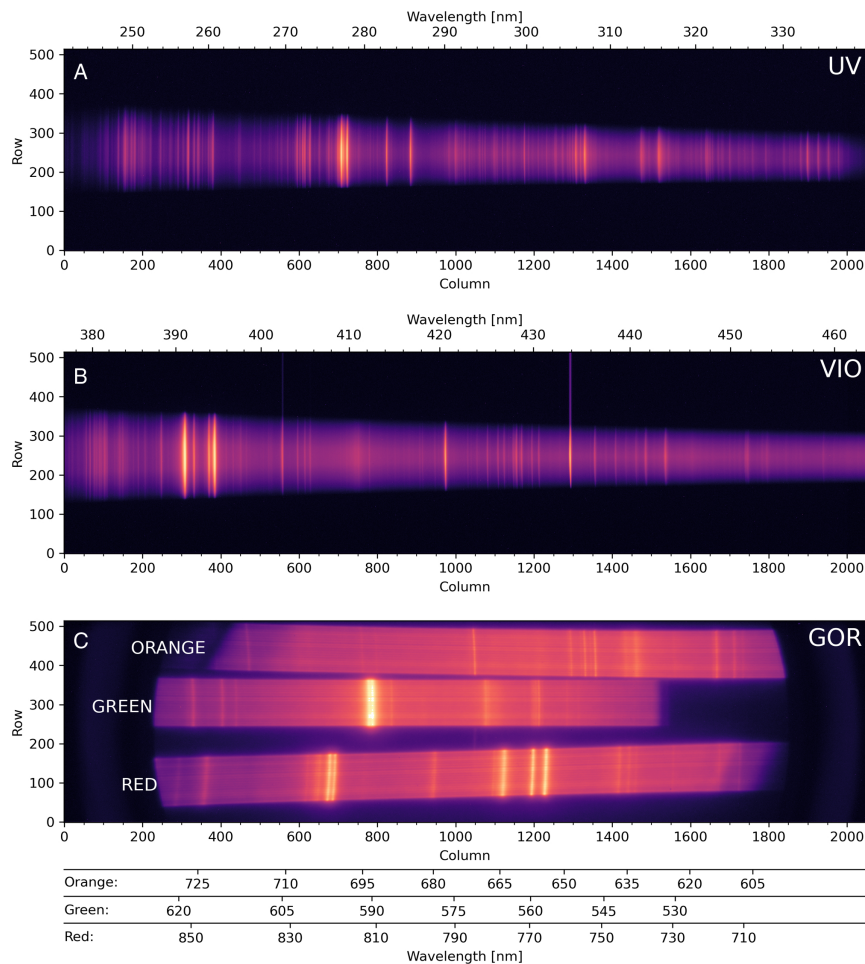

Fig. 2. Log intensity of a 2D readout of a LIBS spectrum of an andesite composition standard. The vertical lines above the illuminated band on the VIO CCD are due to smearing of the room light emission lines during readout. Modified from Figure 12 of [2]. Reproduced under the terms of the Creative Commons CC BY license (https://creativecommons.org/licenses/by/4.0/).

necessary to reduce the number of integration rows to prevent saturation for those regions. However, in the red region, due to the slight tilt of lines with a constant wavelength with respect to the pixel columns on the CCDs, there is a minor improvement in spectral resolution when using fewer rows at the expense of some signal intensity. The green region is fixed at 120 rows, and the orange region is fixed at 128 rows.

During an observation, the readout sequence starts with the UV and VIO CCDs shifting charge "vertically" down the columns at a rate of one shift every 17.99 µs. Initially, the dump gate drains the serial register so that no charge is accumulated there. At the commanded time, the charge transferring process is stopped to allow collection of the signal on the pixels within the illuminated band (the observation itself). Once integration is complete, the CCDs shift the pixels between the serial register and the signal region into the serial register, while the dump gate prevents accumulation. The dump gate is then disabled, and the pixels containing the signal to be summed are shifted into the serial register. CCD vertical transfer then stops, and the serial register is read at a rate of one pixel every 2.5 µs, beginning and ending with 50 "blind" pixels with no corresponding columns on the CCD face and the 2048 image pixels between (see Fig. 34 of ref. [2]). This process is slightly altered for the transmission spectrometer CCD. The phosphor on the intensifier has a characteristic decay lifetime of approximately 4 ms. The intensifier must be dark when the charges are transferred to avoid smearing the signal across the CCD. In order to allow this glow to fade, the CCD integrates for an additional 5 ms after the intensifier shuts off before transferring the signal. Additionally, we need to sequentially sum and read the three separate regions on the transmission spectrometer. The result of this readout process is a set of five spectra (UV, VIO, and GOR) recorded as 1D arrays of length 2148 (50 blind, 2048 image, and 50 blind pixels).

This process results in a variable amount of dark current being collected, along with the spectra, that depends not only on the length of integration time, but also on the number of rows being read out and the position of those rows on the CCD (e.g., the orange region has to wait to be read out after the red then green regions; therefore, the resulting spectrum contains proportionally more dark current). Additionally, the UV and VIO spectrometers do not have any form of shutter to block out light. Consequently, light is still incident on the illuminated rows of the CCDs during readout. These effects were taken into account as described in the methods section below.

C. Calibration Lamps

We used two calibrated lamps as the sources during the calibration campaign. The first was a Labsphere USS-1200S, and the second was a Hamamatsu EQ-99X-CAL (referred to hereafter as the "Labsphere" and the "EQ-99", respectively). The Labsphere consists of an integrating sphere illuminated by four halogen lamps. Calibrated spectral radiance data were provided from the manufacturer for 26 wavelengths between 300 and 2450 nm with a calibrated total relative uncertainty between 0.88 and 3.65% over the VIO and GOR spectral ranges.

The EQ-99 is a laser-driven plasma light source. The plasma is approximately 140×60 µm in size and is visible through a protective window on the front of the lamp. Calibrated spectral

irradiance data for 141 wavelengths from 200 to 900 nm were provided by the manufacturer for a reference surface of 20 cm from the front of the lamp. Over the SuperCam spectral range, the total relative uncertainty ranges from 3.14% to 5.53%. Since the EQ-99 is effectively a point source at any reasonable distance, it does not fill the field of view (FOV) of the telescope, leading to difficulty ensuring that the calibration acquired was representative of the instrument. For this reason, it was only used to calibrate the UV spectrometer–at wavelengths for which the Labsphere has insufficient brightness–and to derive scaling relationships (but not spectral shapes) in other regions. For comparison, the ChemCam instrument was calibrated using the same Labsphere lamp with that instrument's two spectrometers covering the equivalent of SuperCam's VIO and GOR spectral ranges, and a UV fiber lamp was used for the UV range [7].

Here we present a description of the optical calibration of the instrument conducted after integration into the rover at NASA JPL's Spacecraft Assembly Facility. This calibration accounts for the reflectance, transmission, amplification, and/or response of all elements of the instrument from the telescope's protective window [1] to the CCDs.

2. METHODS

A. Data Collection

Instrument optical response data were collected during two shifts at NASA JPL's Spacecraft Assembly Facility in August and December 2019. In August, 30 observations were collected at a range of 10 m using the EQ-99, interspersed with 30 "darks" where the light source was covered with a matte black-anodized aluminum plate. Room lights were required to be on during the calibration for safety reasons, but were turned to the minimum allowed brightness. In December, 10 light/dark pairs were collected using the Labsphere at a range of 5 m, along with an additional 35 light/dark pairs with the EQ-99 at 5 m. The instrument was at room temperature (approximately 25–30 °C) in both cases. Satisfactory alignment and focus were verified through the use of the RMI camera which is co-boresighted with the BU spectrometers.

Each observation consisted of 30 individual spectra from all five spectrometer regions followed immediately by another set of 30 spectra with a slightly longer integration time, repeated for a set of five observations. In these groups of five, the number of CCD rows and intensifier gain settings were held constant, while the integration time was varied, usually over approximately two orders of magnitude. After each group of five, the black aluminum plate was placed in front of the light source, and the group of five repeated with the same settings as before to collect a set of equivalent "dark" observations. Due to time limitations, all row and gain setting combinations were not observed with both lamps.

B. Wavelength Calibration Method

Wavelength calibration was calculated using a LIBS spectrum of a titanium plate and two calibration targets (an ilmenite/hematite mixture, and a clinozoisite, quartz, and orthoclase mixture) collected during the system thermal test in October 2019. The known positions of 535 emission lines for Na, Al, Si,
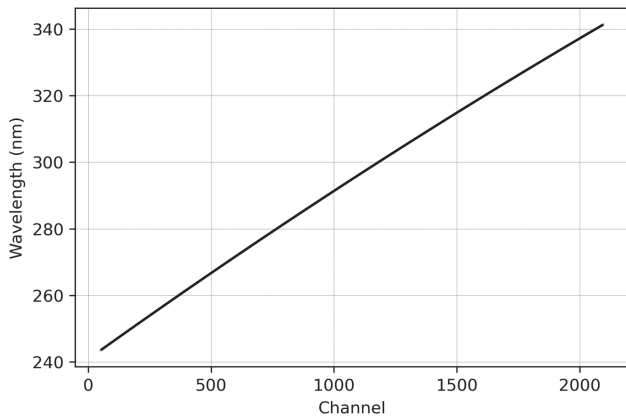
Fig. 3. Wavelength versus the channel number for the UV spectrometer. The channel number is plotted starting at 50 to allow for the 50 blind pixels that precede the 2048 image pixels.
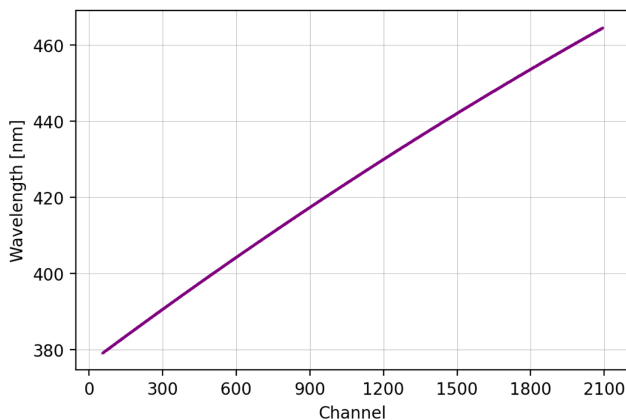

Fig. 5. Wavelength versus the channel number for the GOR spectrometer regions. The gray regions on each series represent unused or unilluminated columns. The inner portions of each series are colored to match the name of the region and denote the used channels.

Fig. 4. Wavelength versus the channel number for the VIO spectrometer. The channel number is plotted starting at 50 to allow for the 50 blind pixels that precede the 2048 image pixels.

Fig. 6. Spectral bin width versus the CCD channel number for the UV spectrometer.

K, Ca, Ti and Fe were mapped to pixel positions on the CCD (Figure S1 in Supplement 1), and a continuous wavelength distribution was fit to this map using a cubic spline. The procedure is described in section 2.3.3 of [7] and has been in use with ChemCam since 2012. Figures 3–5 show the wavelength calibrations for the UV, VIO, and GOR regions, respectively. The wavelength calibration results are included in Data File 1, Data File 2, Data File 3, Data File 4, and Data File 5.

The spectral bin width varies with the wavelength due to a combination of spectrometer geometry and focusing optics. The spectral bin width is calculated by taking the derivative of the wavelength calibration files. Figures 6–8 show the spectral bin widths for the UV, VIO, and transmission spectrometer regions, respectively.

Fig. 7. Spectral bin width versus the CCD channel number for the VIO spectrometer.

C. "Difference of Differences" Technique

Each observation consists of 30 individual spectra taken in rapid succession with the same settings. Since the instrument response function (IRF) data were collected with the spectrometers at room temperature, we discarded the first of these 30 spectra to avoid a spurious signal due to excessive dark current that is cleared by the first readout 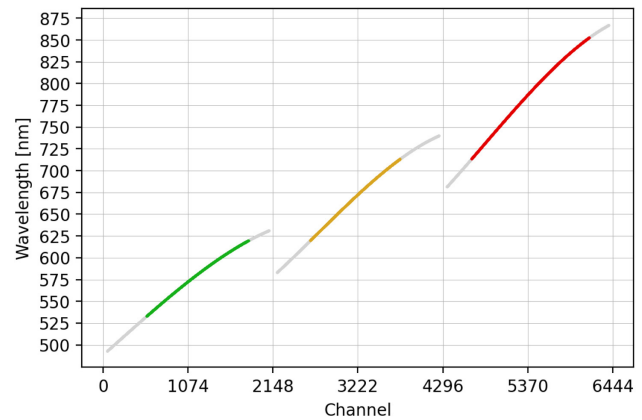of the CCD. We then take the mean of the remaining 29 spectra and perform all later calculations using the mean. Then, in order to remove the portion of the recorded signal due to dark current and readout, we performed a simple two-step correction, as used with ChemCam [7].

First, each mean dark observation was subtracted from the corresponding light one. This removed the portion of the

Fig. 8. Spectral bin width versus the CCD channel number for the GOR spectrometer regions. The gray regions on each series represent unused or unilluminated columns. The inner portions of each series are colored to match the name of the region and denote the used channels.
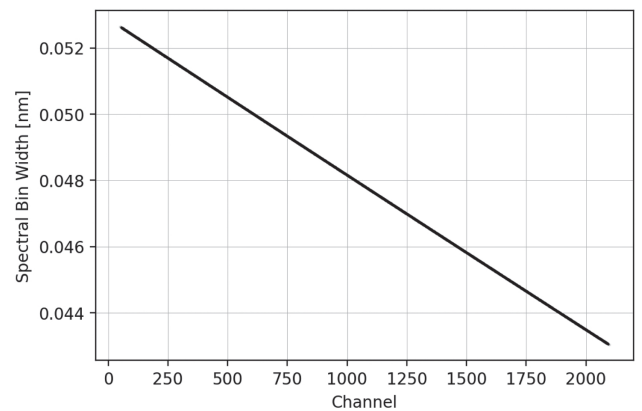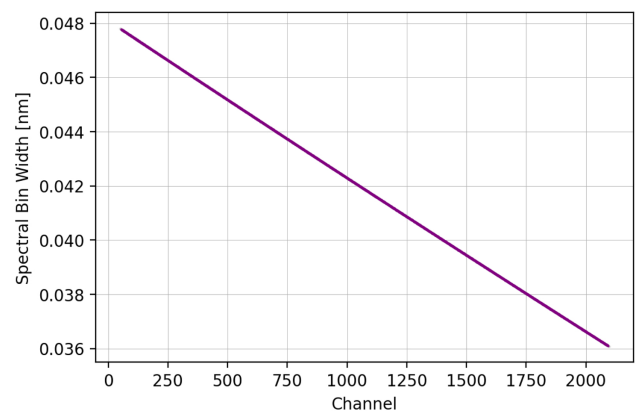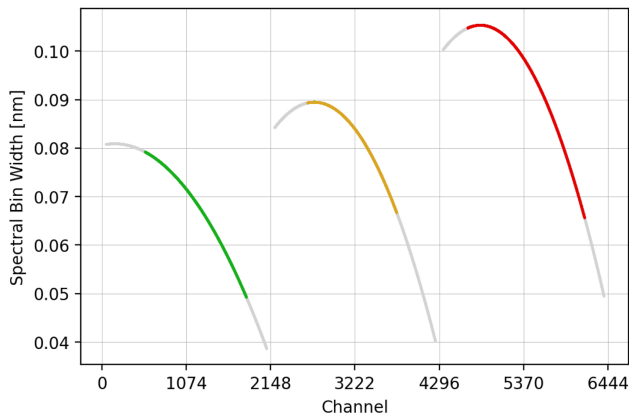

Fig. 9. Comparison of the polynomial fit used for interpolation with the provided calibration data for the Labsphere lamp. The vertical black lines show the wavelength region covered by the GOR spectrometer regions, the blue line is the polynomial fit, and the red crosses are the provided calibration data.

Fig. 10. FOV for the BU spectrometers with requirements indicated in red (0.8 mrad). Altered from Figure 51 of [1]. Reproduced under the terms of the Creative Commons CC BY license (https://creativecommons.org/licenses/by/4.0/).

recorded signal due to dark current on the CCD. Next, we set up pairs of observations within each group of five observations collected with the same CCD row and intensifier gain settings and subtracted the observation with a shorter integration time from the longer one. Since the same CCD row settings were used in both observations, a readout time-dependent signal was constant between them. Thus, assuming a constant light source radiance, constant instrument response, and constant rate of dark current accumulation (i.e., temperature), the signal left after performing this step was due solely to the photons reaching the instrument in the length of time represented by the difference between the longer and shorter integration times. Every possible "longer"-minus-"shorter" combination of the five observations was used to calculate a different result, resulting in 10 estimates for the rate of signal accumulation from each set of five observations (5-4, 5-3, 5-2, 5-1, 4-3, 4-2, 4-1, 3-2, 3-1, and 2-1). In some cases, the longer observations were saturated for some spectrometer regions. Combinations that would include a saturated observation for a region were excluded by checking for the maximum value in each region and flagging the data as saturated if the maximum was greater than 64400 DN (digital number, or counts). Saturation occurs slightly below 2^{16} due to a correlated double sampling routine used in the A–D conversion process [2]. Additionally, some shorter observations were too short to collect a sufficient signal to be useful. Due to the inability to cool the detectors as is normally done on Mars, the dark noise far exceeded the read noise, limiting the utility of short-duration exposures. These observations were also excluded on a per-observation and per-spectrometer-region basis. The general method was to include as many of the collected observations as possible and then remove the ones with the highest noise until the resulting mean of the calculated IRFs had a standard deviation less than 3% of the mean.

D. Instrument Optical Response Calculation

The desired result of the optical calibration is an IRF that maps the signal recorded by the CCD (units of DN) to the photons incident on the limiting aperture of the telescope for each column of pixels on the CCD.
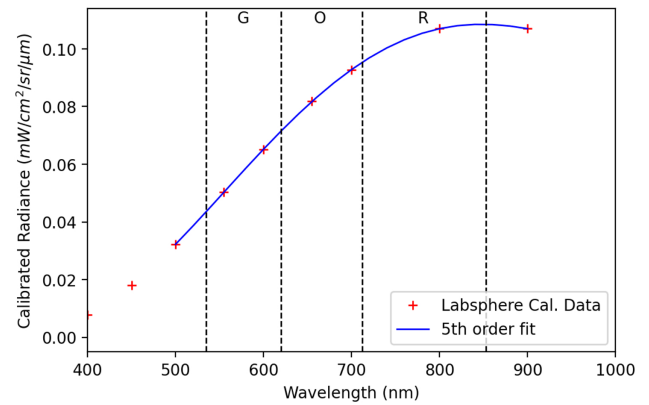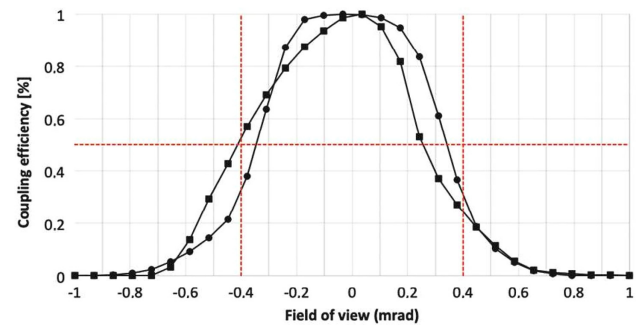
Using a method similar to [8] and starting from the Labsphere calibration data (spectral radiance in units of $mW/cm^2/sr/\mu m$, Data File 6), we can derive the number of photons entering the telescope. First we fit a fifth-order polynomial (to approximate the shape of a Planck curve, given that the Labsphere is a thermal source) to the calibration data in the region of interest (generally from one calibration point before the wavelength range to one point after the wavelength range). The fit was checked to ensure a less than 1% mismatch between the polynomial and the provided calibration data at each calibration wavelength. Figure 9 shows an example of the calibration data with the polynomial fit used for the GOR regions superimposed.

Next, we converted the power term to photons/s at each wavelength using a simple $E = hc/\lambda$ conversion. This results in units of $photons/s/cm^2/sr/\mu m$. Multiplying by the accumulation time from the difference of differences method results in units of $photons/cm^2/sr/\mu m$. Similarly, multiplying by the spectral width of each pixel in micrometers leaves $photons/cm^2/sr$. Next, we must account for the FOV of the telescope and the solid angle subtended by the telescope with respect to the calibration lamp. We had previously determined the FOV of the telescope to be 0.67 mrads in the horizontal axis, and 0.70 mrads on the vertical (Fig. 10 and Fig. 51 of [1]).
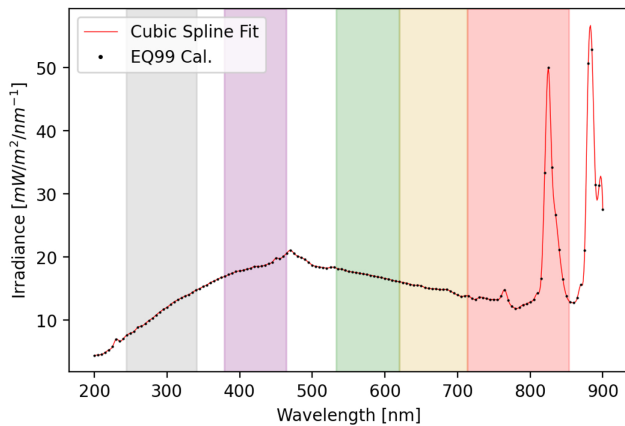
Fig. 11.   EQ-99 calibration data and cubic spline fit used for interpolation. The colored bands on the background represent the UV, VIO, and GOR spectrometer regions from left to right.

We used 0.685 mrads for these calculations. With that value and the distance to the target (d), we can calculate the area on the target using $A = \pi(\text{FOV} \cdot (d/2))^2$.

Multiplying by the area of the FOV on the target leaves units of photons/sr. Finally, the solid angle subtended by the telescope (Ω) depends on the limiting aperture (a) and distance to the target

$$\Omega = \pi \cdot \sin\left(\tan^{-1}\left(\frac{a}{2d}\right)\right)^2. \qquad (1)$$

The limiting aperture for the telescope depends on distance. Since the front aperture of the telescope is slightly smaller than the primary mirror (104 versus 110 mm [1]), targets that are within 2.55 m of the telescope "see" the full primary mirror and have a limiting aperture of 110 mm. Targets that are farther away "see" the primary mirror slightly occluded by the front aperture and have a limiting aperture of 104 mm. Since all optical calibration data were collected at distances of 5 or 10 m, the limiting aperture is 104 mm for this dataset.

Multiplying the data by the solid angle reduces the units to photons, and we can divide the recorded signal by this number for each wavelength to arrive at the IRF in units of DN/photon.

The process for the EQ-99 was similar, except that the calibration data were provided in terms of spectral irradiance (mW/m^2/nm, Data File 7) on a reference surface 0.2 m from the front of the lamp. Since the calibration data for the EQ-99 were provided at a much higher spectral resolution, we used a cubic spline fit provided by the scipy.interplolate. CubicSpline library [9] to interpolate the data between the provided points. A comparison of the provided data and the cubic spline fit is shown overlaid on the spectrometer regions in Fig. 11. We scaled this by $1/r^2$ for the distances used in the calibration campaign multiplied by the area of the controlling aperture, the spectral bin width, and the conversion from power to photons as described above.

4. RESULTS AND DISCUSSION

Preliminary versions of the IRFs were published in [2]. The versions published here differ due to an updated wavelength calibration (average difference between the wavelength calibration

versions of 0.03% and a maximum difference of 0.6% at the short wavelength end of the green region) and due to a software bug, which resulted in the incorrect calculation of the previously reported VIO IRF.

A. UV IRF

The UV IRFs calculated using data collected in August 2019 did not match the data collected in December. Figure 12 shows the ratio of the data as a function of channel. Upon detailed examination of the data and documentation, we determined the position of the EQ-99 plasma within the BU FOV to be slightly different. In August, the plasma was halfway from the center to the left edge of the FOV while, in December, it was nearly at the top edge. Since the EQ-99 is effectively a point source, this meant that we were actually sampling slightly different paths through the instrument. Since it was impossible to collect more measurements of this distribution of paths, it was decided that the best estimate would be to take the mean of these observations and proceed with the rest of the calibration.

The types of data collected in the two campaigns were not completely redundant. In August, we collected data with 16 and 200 rows in the UV. In December, we collected data with 16, 40, and 200 rows, but all of the 200-row data were saturated due to the closer distance of the lamp in the latter campaign. We determined that although the shapes were different between the different sessions, the total signal difference due to the number of rows collected was consistent. To calculate a consistent set of IRFs, we used the mean of the August and December 16-row IRFs, and then scaled it by the December (40-row IRF/16-row IRF) ratio and the August (200-row IRF/16-row IRF) ratios. This estimate has proven to be sufficiently accurate for quantitative LIBS [3]. The final UV IRFs are shown in Fig. 13.

B. VIO IRF

The VIO IRF was calculated using the 200-row data collected with the Labsphere in December. This was scaled to 16 and 40 rows using the EQ-99 data collected in both August and December in the same manner as the UV IRF. Figure 14 shows the final VIO IRFs.
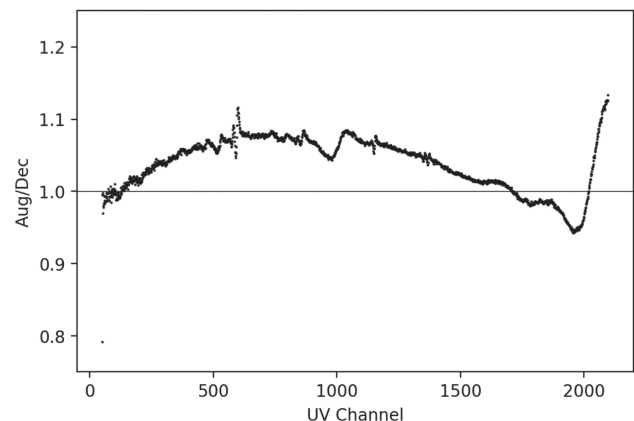

Fig. 12.   Ratio of an IRF calculated for the UV region using data from August 2019 divided by an IRF calculated from data collected in December 2019. The difference is likely due to slightly different positioning of the EQ-99 plasma within the FOV of the telescope.
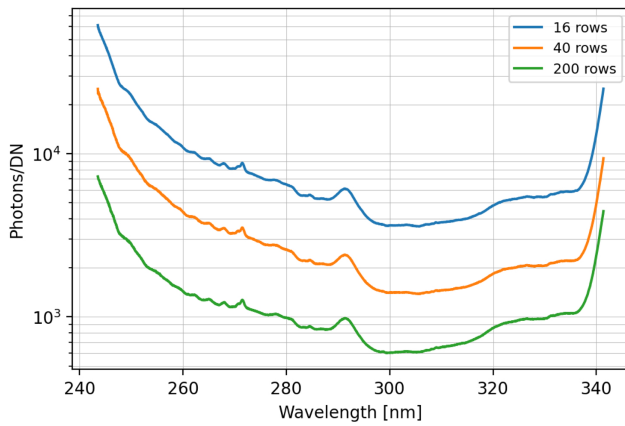
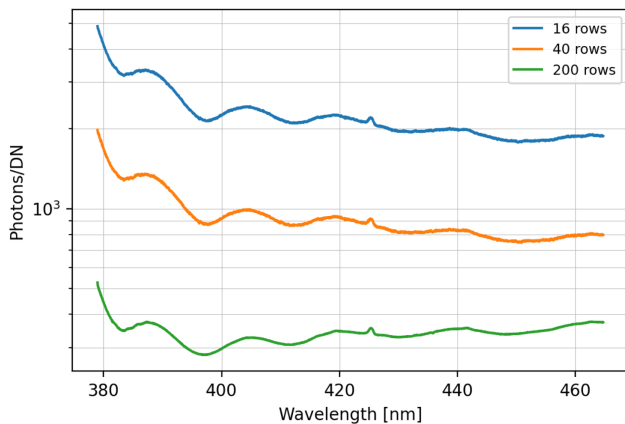**Fig. 13.** Final IRFs used for the UV spectrometer for 16 rows (top), 40 rows (middle), and 200 rows (bottom).

Fig. 14. Final IRFs used for the VIO spectrometer for 16 rows (top), 40 rows (middle), and 200 rows (bottom).

C. Transmission Spectrometer IRFs

The transmission spectrometer calibration data were collected at gains of 2500 and 3200. Since we intended to use more than just those two settings, we derived a gain scaling curve from previous testing of the BU prior to integration onto the rover. This data were collected with the engineering qualification model of the MU attached to the flight BU. Since we are only comparing the amount of amplification from the intensifier, the difference can be ignored. This is acceptable and transferable to the integrated flight model because the quantity we wanted to calculate relies on the intensity of light incident on the intensifier, the number of rows used in the red region, and the intensifier gain setting. We calculated the ratio of the sums of the signals in the usable ranges of each of the spectrometer regions between the different gains and then regressed a second-order exponential fit. The result of that fit is the curve shown in Fig. 15. This scaling function was verified for each spectrometer region individually, as well as all three regions simultaneously. The worst error for the individual regions was for the green region at a gain of 2900 with an error of approximately 6.7%, and the worst error for all regions simultaneously was 2.8%, also at a gain of 2900.

The IRF for the red region using 200 rows was not measured directly with the Labsphere due to the very limited amount of
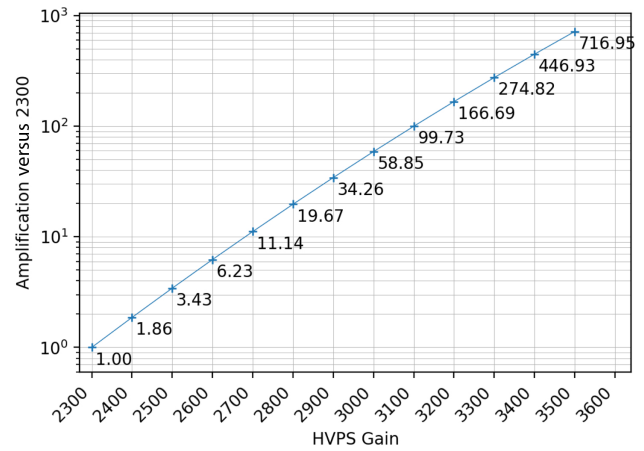

Fig. 15. Amplification factor relative to 2300 gain for various high voltage power supply (HVPS) gain settings for the intensifier used in the GOR spectrometer. The signals in the usable regions of the GOR regions were summed and ratioed to the sum of the signal collected with 2300 gain.
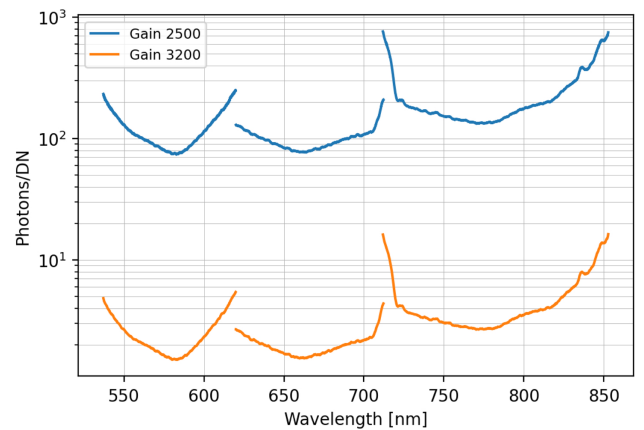

Fig. 16. Final IRFs used for the GOR spectrometer regions for HVPS gain settings of 2500 (top) and 3200 (bottom).

time allowed for calibration on the rover, and sharp features in the EQ-99 spectrum in that range prevent the direct calculation of an IRF from that source. (The calibration data do not adequately describe the sharp features.) However, the ratio of the signal for 200 rows divided by 70 rows was a smooth function and was applied as a scaling factor to the 70-row IRF when needed for observations using 200 rows. The final IRFs for the transmission spectrometer regions are shown in Fig. 16.

The optical calibration presented here has been in use with SuperCam since landing at the Jezero Crater on Mars, on 18 February, 2020. While a number of estimates had to be used in place of direct measurements due to time constraints leading up to launch, the calibration has proven sufficient for quantitative LIBS [3]. The optical IRF described in this paper continues to be used for spectroscopic measurements of Mars geologic and atmospheric targets, the results of which are being prepared for publication at the time of writing.

Supplemental document. See Supplement 1 for supporting content.

REFERENCES

1. S. Maurice, R. C. Wiens, P. Bernardi, *et al.*, "The SuperCam instrument suite on the Mars 2020 rover: science objectives and mast-unit description," Space Sci. Rev. **217**, 47 (2021).
2. R. C. Wiens, S. Maurice, S. H. Robinson, *et al.*, "The SuperCam instrument suite on the NASA Mars 2020 rover: body unit and combined system tests," Space Sci. Rev. **217**, 4 (2021).
3. R. B. Anderson, O. Forni, A. Cousin, *et al.*, "Post-landing major element quantification using SuperCam laser induced breakdown spectroscopy," Spectrochim. Acta B **188**, 106347 (2022).
4. T. Fouchet, J. M. Reess, F. Montmessin, *et al.*, "The SuperCam infrared spectrometer for the Perseverance rover of the Mars 2020 mission," Icarus **373**, 114773 (2021).
5. C. Royer, F. Poulet, J. M. Reess, C. Pilorget, V. Hamm, T. Fouchet, S. Maurice, O. Forni, P. Bernardi, F. Montmessin, L. Lapauw, J. Parisot, M. Bonafous, O. Gasnault, and R. C. Wiens, "Pre-launch radiometric calibration of the infrared spectrometer onboard SuperCam for the Mars2020 rover," Rev. Sci. Instrum. **91**, 063105 (2020).
6. R. C. Wiens, S. Maurice, B. Barraclough, *et al.*, "The ChemCam instrument suite on the Mars Science Laboratory (MSL) rover: body unit and combined system tests," Space Sci. Rev. **170**, 167–227 (2012).
7. R. C. Wiens, S. Maurice, J. Lasue, *et al.*, "Pre-flight calibration and initial data processing for the ChemCam laser-induced breakdown spectroscopy instrument on the Mars science laboratory rover," Spectrochim. Acta B **82**, 1–27 (2013).
8. J. R. Johnson, J. F. Bell, S. Bender, D. Blaney, E. Cloutis, L. DeFlores, B. Ehlmann, O. Gasnault, B. Gondet, K. Kinch, M. Lemmon, S. Le Mouelic, S. Maurice, M. Rice, R. C. Wiens, and M. S. Team, "ChemCam passive reflectance spectroscopy of surface materials at the Curiosity landing site, Mars," Icarus **249**, 74–92 (2015).
9. P. Virtanen, R. Gommers, T. E. Oliphant, *et al.*, "SciPy 1.0: fundamental algorithms for scientific computing in Python (vol. 33, pg 219, 2020)," Nat. Methods **17**, 352 (2020).